Mapping the Exciton Diffusion in Semiconductor Nanocrystal Solids

Natalia Kholmicheva,[†,‡] Pavel Moroz,[†,‡] Ebin Bastola,[‡,§] Natalia Razgoniaeva,[†,‡] Jesus Bocanegra,[∥] Martin Shaughnessy,[∥] Zack Porach,[⊥] Dmitriy Khon,[∥] and Mikhail Zamkov*[,†,‡]

[†]The Center for Photochemical Sciences, [‡]Department of Physics, and [⊥]Department of Chemistry, Bowling Green State University, Bowling Green, Ohio 43403, United States, [§]Department of Physics, University of Toledo, Toledo, Ohio 43606, United States, and [∥]Department of Chemistry and Biochemistry, St. Mary's University, San Antonio, Texas 78228, United States

ABSTRACT Colloidal nanocrystal solids represent an emerging class of functional materials that hold strong promise for device applications. The macroscopic properties of these disordered assemblies are determined by complex trajectories of exciton diffusion processes, which are still poorly understood. Owing to the lack of theoretical insight, experimental strategies for probing the exciton dynamics in quantum dot solids are in great demand. Here, we develop an experimental technique for mapping the motion of excitons in semiconductor nanocrystal films with a subdiffraction spatial sensitivity and a picosecond temporal resolution. This was accomplished by doping PbS nanocrystal solids with metal nanoparticles that force the exciton dissociation at known distances from their birth. The optical signature of the exciton motion was then inferred from the changes in the emission lifetime, which was mapped to the location of exciton quenching sites. By correlating the metal–metal interparticle distance in the film with corresponding changes in the emission lifetime, we could obtain important transport characteristics, including the exciton diffusion length, the number of predissociation hops, the rate of interparticle energy transfer, and the exciton diffusivity. The benefits of this approach to device applications were demonstrated through the use of two representative film morphologies featuring weak and strong interparticle coupling.

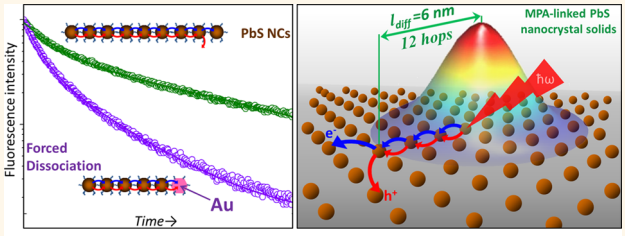

KEYWORDS: charge transport · thin films · plasmonics · colloidal quantum dots

Solution processing of semiconductor nanocrystal (NC) solids represents a promising strategy for the development of novel optoelectronic applications. An important advantage of these materials lies in the spectral tunability of their optical properties, which results from the quantum confinement of photoinduced charges. The colloidal stability of semiconductor NCs offers another important benefit, as it enables low-cost solution processing of thin films virtually on any substrate. The electrical conductivity of quantum dot solids is typically rendered through the use of short molecular linkers,[1−6] or encapsulating matrices[7−10] that preserve some degree of quantum confinement while promoting an electrical coupling between neighboring nanoparticles. So far, this strategy has been rewarded through the development of high-performance materials for light-emitting[11−18] and photovoltaic[19−34] applications. Nevertheless, despite an ongoing improvement in the function of NC-based devices, the electrical transport in semiconductor NC films remains to be the subject of an active debate.[35,36] Controversial viewpoints arise from the fact that the basic processes of exciton and carrier diffusion in nanoparticle solids cannot be easily imaged. In light of this limitation, novel experimental tools offering both spatial and temporal sensitivity are in great demand.

It is generally accepted that photoexcitation of NC films leads to the formation of localized excitons that diffuse into a solid at rates determined by the strength of the interparticle coupling.[37] Similar to the exciton dynamics of polymer films, a bound electron–hole pair in a NC solid will diffuse until reaching a potential energy minimum, which could result in its recombination or dissociation. The exact mechanism of the exciton decay depends on several morphological parameters and is highly important to the performance of ensuing NC devices.[35,38] For example, the exciton diffusion toward film boundaries in quantum dot

* Address correspondence to zamkovm@bgsu.edu.

Received for review December 5, 2014 and accepted February 15, 2015.

Published online February 16, 2015
10.1021/nn507322y

light-emitting diodes causes quenching of the luminescence, which limits the device efficiency.[39] On the contrary, the diffusion of excitons to charge-separating interfaces in NC solar cells is highly beneficial as it leads to the generation of photocurrent.[37] These and other examples confirm that the knowledge of exciton dissociation processes is central to the NC device design.[35] Ideally, the rates of these processes should be controlled toward improving the desired functionalities of NC assemblies.

A unique feature of excitons in NC solids concerns their relatively low binding energy. Unlike polymer films, in which the dissociation of excitons occurs only at interfaces of different material phases, the splitting of bound electron−hole pairs in NC solids can be triggered by less energetic processes, such as charge tunneling between neighboring NCs.[40] The emerging free carriers will then drift through the solid with mobilities that depend on the strength of interparticle coupling, as was confirmed by numerous studies of charge transport dynamics in NC solids.[41−46] Studying the motion of neutral excitons, however, is a far more challenging task. To date, the exciton diffusion in NC solids has been investigated *via* steady-state and time-resolved spectroscopy methods[36,44,47−52] while their diffraction limited spatial profile has been visualized through optical microscopy.[35] Despite these efforts, the exact nature of the exciton dissociation mechanism as well as exciton diffusion trajectories in NC solids still remains poorly understood.

Here, we map the spatial and temporal dynamics of the energy transport processes in PbS NC solids by forcing the exciton dissociation at known distances from their birth. This was achieved by doping the NC film with Au nanoparticles that induce the nonradiative recombination of carriers.[53,54] Within this approach, the optical signature of the exciton dissociation (splitting) events was inferred from the changes in the lifetime of the Au-doped PbS NC emission, which was mapped to the location of exciton quenching sites. The experimental data were then compared to the predictions of a random walk diffusion approximation aimed to establish the correlation between the changes in the exciton lifetime and the density of Au domains in a film. By applying this strategy to PbS NC solids, we found that the probability of the exciton dissociation per single interparticle hop is p_{diss} (1 hop) = 9%, if PbS NCs are linked with short-chain 3-mercaptopropionic acid (MPA) ligands, p_{diss} (1 hop) = 3% when longer-chain 8-mercaptooctanoic acid (MOA) molecules are used. In the case of MPA-linked solids (interparticle distance = 0.9 nm), excitons diffused to an average length of 5.7 nm in approximately 12 hops, which corresponded to the diffusion mobility (diffusivity) of 0.012 $cm^2\ s^{-1}$. Meanwhile, MOA-linked solids (interparticle distance = 1.7 nm) gave rise to a longer diffusion length of 11.4 nm (34 hops) and a lower diffusivity of 0.003 $cm^2\ s^{-1}$. The observed difference in the dynamics of the two film types was found consistent with the proposed charge-tunneling mechanism of the exciton dissociation.

To reveal the nature of exciton dissociation processes the fluorescence (FL) lifetime data were complemented with the steady-state emission measurements of Au-doped PbS NC films. On the basis of the observed relationship between the density of Au NPs and the ensuing PbS emission wavelength we were able to conclude that the exciton dissociation process is likely to be induced by interdot charge tunneling rather than carrier scattering on defects. Another interesting trend was inferred from the comparison of nanoparticle solids utilizing different architectures. Measurements of the exciton diffusion lengths in MPA- and MOA-passivated NC films allowed the determination of the effect of the interparticle distance on the energy transfer (ET) rate. The observed ET distance dependence suggested a possible deviation from Förster scaling, indicating the presence of the nondipolar contribution into exciton coupling in NC films. This phenomenon was previously observed by Tisdale[36] and others[55] and was ascribed to the effect of a nanoparticle size, which does not conform the point dipole approximation. In addition to studying the exciton diffusion processes, the developed model was complemented with the time-resolved measurements of free carrier recombination, which further contributed to elucidating the energy relaxation dynamics in PbS NC solids.

RESULTS AND DISCUSSION

The fluorescence intensity decay is emerging as a viable tool for "non-contact" measurements of the excited state dynamics in semiconductor NC solids.[40,44,48,56−59] To date, this strategy has been used primarily for monitoring the downhill migration of excitons in a film, providing important insights into the carrier recombination dynamics. Recently, the emission intensity decay approach was adapted toward distinguishing between the recombination rates of bound and free carriers in a quantum dot solid. This differentiation was achieved by extracting the fast and the slow components of the FL intensity decay in PbS NC solids containing "insulating" ZnS barriers.[44] The presence of ZnS dots in the gaps between PbS NCs enabled the suppression of the interparticle charge transfer, which allowed attributing the fast decay component of the PbS-only NC emission to the exciton dissociation process while the slow exponent was ascribed to free carrier trapping on NC surfaces, as shown in Figure 1.

Despite providing a powerful tool for probing the excited state dynamics in NC solids, the time-resolved emission alone does not offer the spatial resolution needed for imaging the motion of excitons in a

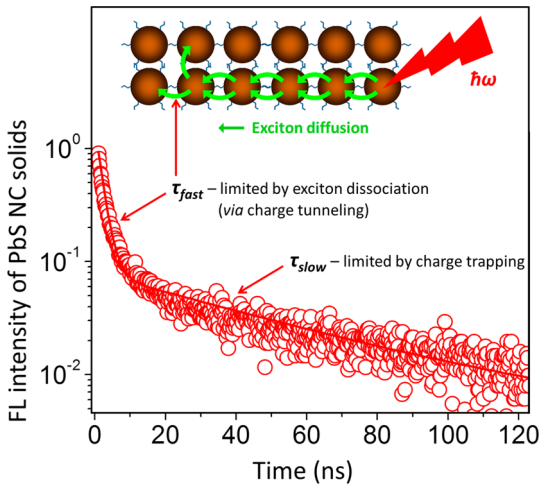

Figure 1. FL intensity decay of semiconductor NC solids often contains two distinct decay components.[44] The fast time reflects the rate of exciton dissociation, which is presumably driven by charge tunneling processes, while the slow exponent is determined by the rate of free carrier trapping on NC surfaces.

three-dimensional film. As a result, a number of important questions concerning the energy relaxation pathways in NC solids still remain unanswered. First of all, it is unclear how far an exciton can diffuse into a solid prior to its dissociation into a free electron–hole pair. The expected diffusion length along with possible exciton trajectories is central to the design of photovoltaic materials, since these parameters determine the ultimate p–n junction geometry and the maximum length of the carrier collection path. Second, knowing mechanisms that trigger the exciton dissociation is likewise important, as these processes can be controlled for on-demand enhancement or suppression of free carrier generation. While it was hypothesized that tunneling of one of the charges is the primary mechanism of exciton splitting,[13] an alternative explanation based on exciton migrating to trap states or nonemissive potential minima (large-diameter NCs) could not be ruled out.

In this work, the subdiffraction mapping of excitons was achieved by doping PbS NC solids with a small amount of Au NPs. Owing to a high density of states in metals, Au dopants promote a nonradiative recombination of excitons, decreasing their lifetime. By correlating the Au–Au interparticle distance in the film with the corresponding change in the FL lifetime, ΔFL, it is therefore possible to obtain the average length of the exciton diffusion, l_{diff}^{exc}, and the number of interparticle hops made by excitons prior to the dissociation, n_{hop}. These two parameters can then be used to derive other important transport characteristics, including the exciton diffusivity and the dot-to-dot energy transfer rate.

To confirm that Au nanoparticles can be used for quenching excitons in semiconductor NC solids, we have carefully examined the emission of mixed (Au, PbS) NC films. In these experiments, Au nanoparticles were electrically coupled into the surrounding "matrix" of PbS NCs though the use of ligands that promote the PbS-to-Au *charge* transfer, causing a nonradiative decay of PbS excitons. We note that quenching of PbS excitons *via energy* transfer to Au is likely to be slow. Indeed, the energy of PbS excitons (1.4 eV) is lower than that of plasmon excitations (2.2 eV), such that the resonant ET is uphill and therefore suppressed while the nonresonant ET is weakened by the poor spectral overlap of Au and PbS NPs at the PbS band gap energy. To introduce Au "dopants" into a PbS NC film, solution-cast films of oleylamine-capped Au and PbS nanoparticles were treated with short-chain MPA molecules. The ratio of Au to PbS NCs in the resulting (Au, PbS) solids was determined from TEM images of mixed (Au, PbS) nanoparticle solutions prior to deposition (see Figure 2 panels a–c). Several films exhibiting the same optical density (at the PbS exciton feature) were fabricated to determine the effective radius of Au NPs that promotes quenching of PbS excitons. According to Figure 2, the emission of (Au, PbS) films is almost fully quenched when the ratio of Au to PbS falls below 2, and is reduced to about 40% when the ratio of Au to PbS is 1:30. The emission loss in (Au, PbS) films, ΔFL/FL, which represents the fraction of "quenched" PbS NCs was then used to determine the effective radius of Au nanoparticles that promotes quenching (see Figure SF1 for details). On the basis of the best model fit (Figure 2d, red curve), we found the effective "quenching" radius to be R_{eff} (Au) ≈ 3.5 nm, which was just slightly larger than the physical size of Au NPs appended with MPA ligands ($R_{physical}$ (Au + MPA) ≈ 3.0 nm). The effective "quenching" radius of Au nanoparticles grew to 3.8 nm when longer-chain MOA ligands were used as interlinking molecules.

The character of exciton diffusion through a uniform NC solid (prior to Au doping) can be viewed as random provided that the energy disorder in the film does not exceed the room temperature *kT*. In this case, the relation between the exciton diffusion length and the number of interparticle hops, n_{hop}, obeys a three-dimensional random walk approximation, $l_{diff}^{exc} = l_{hop}\cdot(n_{hop}/6)^{1/2}$, where l_{hop} is the average center-to-center spacing between adjacent dots (see Supporting Information). By setting the average probability of exciton dissociation per single hop, p_{diss}(1 hop) to be a free parameter, we can express the probability of exciton dissociation on its *n*th hop: $p(n_{hop}) = p_{diss}(1) \times (1 - p_{diss}(1))^{n_{hop}-1}$. The resulting probability distribution (black curve in Figure 3a) reflects the fraction of the exciton population in a solid, $N_{exciton}(n_{hop})$, which remain excited (unquenched) after each hop.

With the introduction of Au NPs into a NC solid, excitons become forced to dissociate at shorter distances, which are related to the Au–Au interparticle separation, R_{Au-Au}. As a result, some of the exciton diffusion volume accessible for PbS-only NC solids will

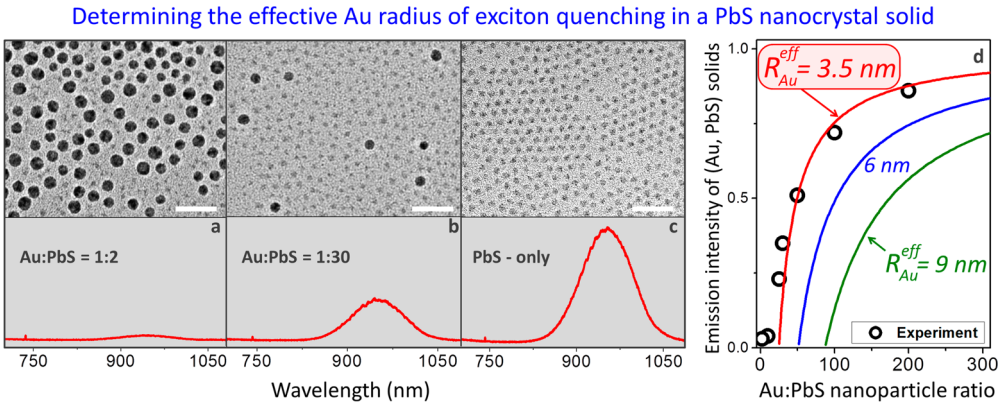

Figure 2. Determining an effective radius of a Au nanoparticle that promotes exciton quenching in a PbS NC solid. (a–c). Transmission electron microscope (TEM) images and the corresponding emission profiles of nanoparticle solids featuring different concentrations of Au. (a) Au:PbS = 1:2 (by nanoparticle count); (b) Au:PbS = 1:30; (c) PbS only solids. (d) The effective radius of a Au nanoparticle that results in quenching of excitons is determined by fitting the experimental data (the emission reduction *versus* Au concentration) with several predicted quenching scenarios, corresponding to R_{eff} = 3.5 nm (red curve), R_{eff} = 6 nm (blue curve), R_{eff} = 9 nm (green curve). Fitting model is described in Supporting Information, Figure SF1.

be restricted when Au NPs are added to the film. This leads to the reduction of the emission lifetime due to the forced electron–hole recombination in a metal nanoparticle. Qualitatively, the emission intensity of NC films featuring a relatively small value of $l_{exciton}^{diff}$ will not be altered significantly upon Au doping, since most excitons in this case will dissociate before reaching Au NPs. Conversely, when the exciton diffusion length is large, the motion of most excitons will be interrupted by the premature recombination on Au, leading to a significant reduction in the emission lifetime, as compared to PbS-only films.

From the quantitative prospective, the emission changes in Au-doped PbS NC films convey the sufficient amount of information needed to determine the probability of exciton dissociation per single interparticle hop, p_{diss}(1 hop). Because radiative recombination of PbS excitons in a solid occurs spontaneously, the total number of emitted photons from a NC film will be proportional to the average lifetime of an exciton and, thus, to the total number of hops, n_{hop}, that excitons make prior to splitting or quenching by gold. Consequently, the number of emitted photons from a NC solid, N^{ph}, will be proportional to the total area under the exciton population decay curve, $N(n_{hop})$, such that $N_{PbS-only}^{ph} = \int_0^{\infty} N(n_{hop})\, dn_{hop} \approx \langle N \rangle \langle n_{hop} \rangle$, as shown in Figure 3a. The emission from a Au-doped film will be reduced due to a restricted diffusion length, $N_{Au-PbS}^{ph} = \int_0^{nmax} N(n_{hop})\, dn_{hop}$. We can then express the expected reduction in the number of emitted photons resulting from Au doping as the ratio of "unshaded" to total area under the decay curve (see Figure 3 panels b and c):

$$\Delta FL_{theor}(p_1^{diss}) = \frac{N_{Au-PbS}^{ph}}{N_{PbS-only}^{ph}} = \frac{area_{unshaded}(p_1^{diss})}{area_{total}(p_1^{diss})} \quad (1)$$

Experimentally, the same reduction can be estimated as the ratio of photons emitted with and without Au present. To distinguish the band gap exciton emission from the contribution of free carriers,[44] we include only the fast decay component of the FL decay into the intensity integration, $I_{FL} = \exp(-t/\tau^{fast})$:

$$\Delta FL_{exp} = \frac{N_{Au-PbS}^{ph}}{N_{PbS-only}^{ph}} \approx \frac{\int \exp(-t/\tau_{Au-PbS}^{fast})\, dt}{\int \exp(-t/\tau_{PbS-only}^{fast})\, dt} = \frac{\tau_{Au-PbS}^{fast}}{\tau_{PbS-only}^{fast}} \quad (2)$$

By setting the theoretical and experimental emission changes equal to each other, $\Delta FL_{theor}(p_1^{diss}) = \Delta FL_{exp}$, we can then determine the probability of exciton dissociation per single step, p_{diss}(1 hop).

Figure 3 panels b and c simulate two possible scenarios of the exciton diffusion through a solid following a single excitation pulse and corresponding to a high (p_{diss} = 0.1; blue) and low (p_{diss} = 0.03; red) dissociation probability per single interparticle hop. The resulting decay population curves (red and blue) show the fraction of undissociated excitons after each hop. The corresponding diffusion length $l_{exciton}^{diff}$ is shown at the top of the plot. The shaded areas in Figure 3 panels b and c represent the exciton population, which is likely to be quenched through a forced recombination with Au nanoparticles. The average scatter-free length of the exciton diffusion, $l_{free\ travel}$, in the presence of Au doping (green dashed line in Figures 3 panels b and c) will be determined by the average distance between Au NPs in the film, R_{Au-Au}, and the effective Au radius for exciton quenching, R_{eff}(Au), as illustrated in Figure 5a. The overall lifetime of a scatter-free diffusion of an exciton in a solid measured between the photoexcitation and the quenching events is given by $\tau_{exciton}^{diss}(n_{hop}) = t_{step} n_{hops}$, where t_{step} is the average nearest-neighbor energy transfer time. Experimentally, the total time of the exciton diffusion (with or without Au present) is given

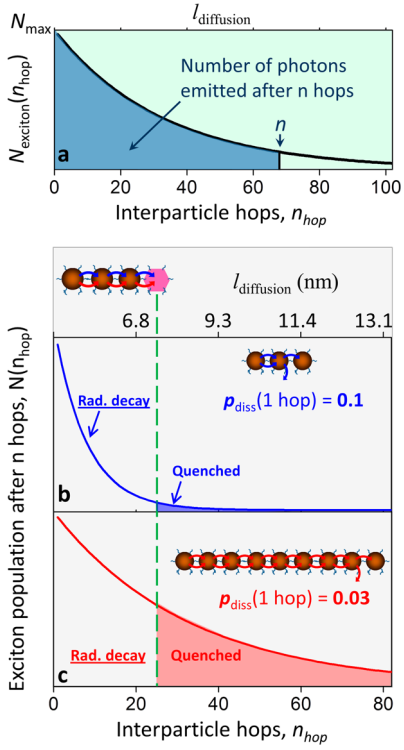

Figure 3. (a). The experimental strategy for determining the exciton diffusion length in a NC solid. Assuming that on every hop, excitons have a certain probability of dissociating, p_{diss}(1 hop), we can simulate the relationship between the exciton population in a film and the number of interparticle hops. The emission from the film is proportional to the exciton lifetime and therefore to the area under the population decay curve, as shown. Using the Einstein relation for the random-walk diffusion in 3D, we can estimate the exciton diffusion length, $l_{diff}^{exciton}(n)$, which is shown in the upper *x*-axis. (b,c). The decay of exciton population in a solid corresponding to the two values of a single-hop dissociation probability: p_{diss}(1 hop) = 0.1 (blue) and p_{diss}(1 hop) = 0.03 (red) is shown. If Au NPs are inserted into a PbS solid, the dissociation of excitons will be forced at shorter distances (see text). This will result in the reduction of the fast component of the PbS emission lifetime. By comparing the ratio of the two areas under the exciton population curve, labeled radiative and nonradiative, to the attenuation ratio of FL lifetimes in Au-doped PbS NC films, the exciton dissociation probability can be determined.

by the fast decay component in the FL intensity decay, $\tau_{exciton}^{diss} = \tau_{fast}^{FL}$.

To determine the exciton diffusion length in ligand-linked PbS NC solids we have fabricated several mixed (Au, PbS) films featuring different concentrations of Au nanoparticles. To this end Au ($d \approx 5.0$ nm) and PbS ($d \approx 3.1$ nm) NCs were mixed in octane at predefined ratios and used as "inks" for processing film layers. For better miscibility the surfaces of both nanoparticle types were passivated with long-chain oleylamine ligands. Upon spincasting of a thin layer, the bulky ligands were exchanged with either 3-mercaptopropionic acid (MPA) or 8-mercaptooctanoic acid (MOA) molecules on each cycle of the layer-by-later (LbL) deposition process. The two ligand types were designed to promote different degrees of PbS interparticle coupling, associated with different rates of exciton hopping through the solid. On the basis of previously performed film analyses *via* grazing-incidence small-angle X-ray scattering (GISAXS) measurements,[13] the partial cross-linking of short-chain MPA ligands gives rise to an interparticle edge-to-edge distance of approximately 0.9 nm, while MOA molecules result in longer gaps of 1.7 nm. The thickness of fabricated films was ranging between 200 and 300 nm.

The fraction of Au nanoparticles in a solid was determined by finding the ratio of Au to PbS NCs in solution. To this end, a colloidal mixture of Au and PbS nanoparticles was deposited onto a TEM grid and analyzed. The ratio of each nanoparticle type (Au *versus* PbS) could be easily obtained by identifying the corresponding populations of each material in a TEM specimen, as shown in Figure 4. The ratio of Au to PbS particles on a TEM grid, n_{TEM}, was then converted to a Au volume fraction, v_{Au}, and the average Au-to-Au interparticle distance, R_{Au-Au}, assuming a simple cubic packing of nanoparticles (see Supporting Information for details of calculation):

$$v_{Au} = \frac{4/3\pi R_{Au}^3}{(\sqrt[3]{n_{TEM}} D_{PbS} + D_{Au})^3};$$

$$R_{Au-Au} = \sqrt[3]{n_{TEM}} D_{PbS} + D_{Au} \qquad (3)$$

A denser packing order of nanoparticles is possible and may result in the reduction of R_{Au-Au}. In the limiting case of closed packed ordering (face cubic centered, fcc), which could form if oily long-chain ligands are used instead of MPA molecules, Au-to-Au interparticle distance becomes R_{Au-Au} (fcc) $\approx 0.89 * R_{Au-Au}$ (simple cubic), as shown in the SI section. Upon the introduction of Au NPs into PbS films, the scatter-free diffusion length of excitons becomes limited to $l_{free\ travel}$ (see Figure 5c and the Supporting Information, Figure SF2, for details of calculation), which represents the mean free path of excitons in a PbS NC solid doped with evenly distributed Au NPs.

The FL intensity decay of PbS NC films featuring several concentrations of Au NPs is shown in Figure 5d. The corresponding "quenching" distances, $l_{free\ travel}$, were determined from the concentrations of Au in each solid and are given in Figure 5c. Expectedly, the longest emission lifetime (black curve) was obtained for PbS-only films for which the exciton diffusion is limited either by charge tunneling (carrier ionization) or exciton trapping at potential minima. The inclusion of Au NPs into PbS NC films resulted in a proportional drop of the FL lifetime, as seen in Figure 5d. Overall, the lifetime of the PbS band gap emission was decreasing in a consistent manner with the growing concentration of Au NPs. A double exponential fit of the FL intensity decay was employed to obtain an accurate estimate of the fast FL component, τ_{fast}^{FL}, corresponding to the exciton lifetime in a solid.

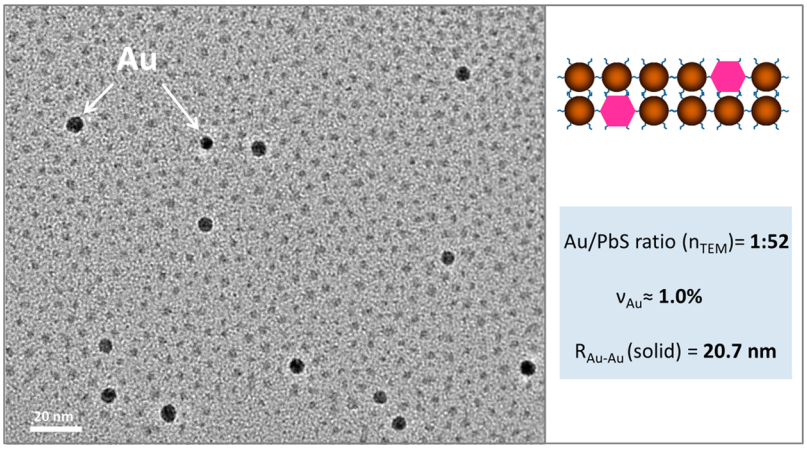

Figure 4. Transmission electron microscope (TEM) image of a mixed (Au + PbS) nanoparticle sample used for developing (Au, PbS) solids. The apparent ratio of Au to PbS nanoparticles on a grid, n_{TEM}, can be used to estimate the ultimate gold-to-gold interparticle distance R_{Au-Au} in a solid. $R_{Au-Au} = n_{TEM}^{1/3} D_{PbS} + D_{Au}$, where D_{PbS} and D_{Au} are the diameters of PbS and Au NPs, respectively.

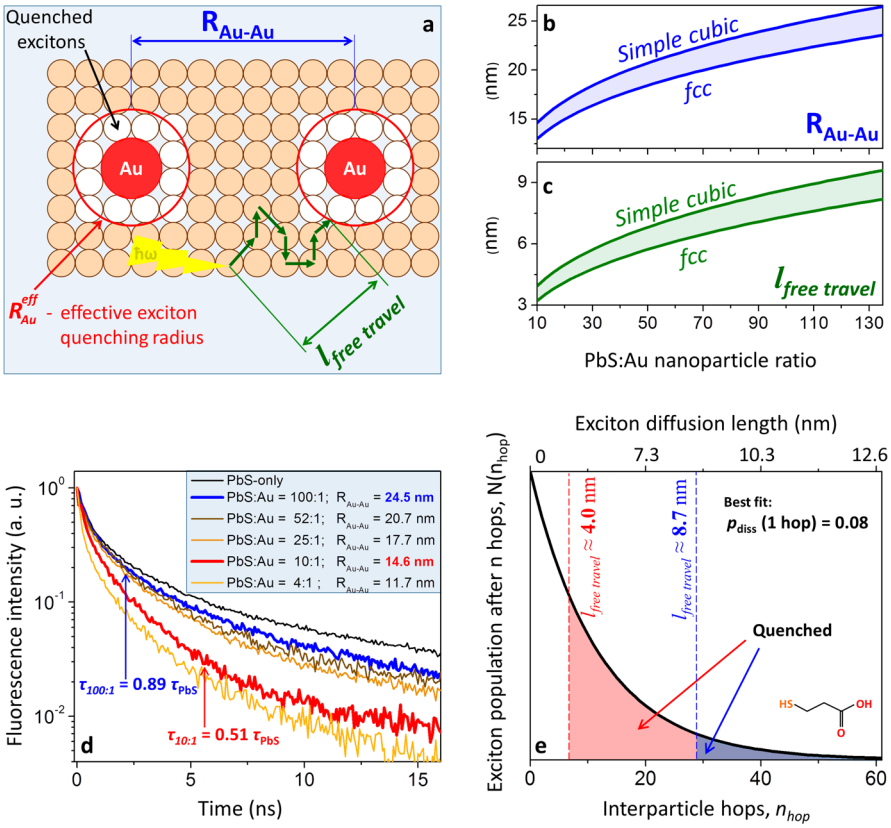

Figure 5. Experimental determination of the exciton diffusion length in MPA-linked PbS NC solids. (a) An illustration of the three characteristic distances in (Au, PbS) solids: the average scatter-free length of the exciton diffusion, $l_{free\ travel}$, the Au−Au interparticle distance, R_{Au-Au}, and the effective Au radius for exciton quenching, R_{eff}(Au). (b) The relationship between R_{Au-Au} and the PbS:Au nanoparticle ratio (see Supporting Information) for simple cubic and fcc packing orders. (c) The relationship between $l_{free\ travel}$ and the PbS:Au nanoparticle ratio (see Supporting Information). (d,e) The attenuation of the fast decay component in the emission of PbS NC solids induced by an increasing concentration of Au NPs (d) can be correlated to the changes in the *unshaded* area under the exciton population curve (e). By modeling the exciton population curve N(p_{diss}(1)), we determined the probability of exciton dissociation on each hop in MPA-linked PbS NC solids (d_{PbS} ≈ 3.1 nm) to be 9%, p_{diss}(1 hop) = 0.09.

To estimate the probability of exciton dissociation per single interparticle hop, p_{diss}(1 hop), the measured reduction in the emission lifetime in Au-doped NC solids, ΔFL_{exp}, was set equal to ΔFL_{theor}. The value of p_{diss}(1 hop) was then determined by finding the best match: $\Delta FL_{theor}(p_1^{diss}) = \Delta FL_{exp}$, conjointly for all investigated (Au, PbS) films. This strategy is illustrated graphically in Figure 5e. The best fit for the observed

TABLE 1. Summary of Exciton Transport Characteristics for PbS-Only NC Solids Obtained Using the Developed Forced Dissociation Approach

type of PbS NC solid	p_{diss}(1 hop)	$\langle n_{hop} \rangle$	$l_{exc.diff.}$ (nm)	$\tau_{FL,fast}$ (ns)	τ_{ET} (ns)	$\mu_{exc\cdot diff.}$ (cm^2/s)
MPA-linked (R_{edge} = 0.9 nm)	0.09	12	5.7	1.1	0.089	0.012
MOA-linked (R_{edge} = 1.7 nm)	0.03	34	11.4	15.1	0.44	0.003

value of ΔFL_{exp} was obtained according to eq 2, by requiring that the ratio of unshaded to the total area under the $N(n_{hop})$ curve was equal to the emission lifetime ratio $\tau_{Au-PbS}/\tau_{PbS-only}$, consistently for all investigated film. The extracted values of p_{diss}(1 hop) are given in Table 1.

We note that each of the several films fabricated using MPA ligands represents an independent measurement of the exciton diffusion length. In principle, a single-concentration measurement of emission quenching is sufficient for determining the transport characteristics. By employing several PbS films featuring different Au concentrations, we estimate the standard deviation of the exciton dissociation probability to be within 10%, as shown in Supporting Information, Table ST1.

For MPA-linked films, the value of the exciton dissociation probability per single interparticle hop was found to be 0.09. Under these conditions the 1/*e* drop in the exciton population is reached after $\langle n_{hop} \rangle$ = 12 hops, which corresponds to the diffusion length of 5.7 nm. Since the total time of the exciton diffusion is given by τ_{fast}^{FL}, we can estimate the exciton diffusivity using the Einstein equation:

$$\mu^{exc} = \frac{el_{hop}^2}{6kT}\frac{1}{\tau} = \frac{el_{hop}^2}{6kT}\frac{\langle n_{hop} \rangle}{\tau_{FL}^{fast}(\text{PbS only})}$$

where l_{hop} is the center-to-center interparticle distance, which in the case of MPA-linked films is estimated to be $2R_{PbS} + 0.9$ nm = 4.0 nm. According to the above equation, the room temperature exciton diffusivity for MPA-linked PbS NC solids is 0.012 $cm^2\ s^{-1}$. Since both the total number of hops ($\langle n_{hop} \rangle$ = 12) and the total diffusion time (τ_{FL}^{fast}(PbS only) = 1.06 ns are known, we can estimate the average rate of energy transfer between neighboring PbS NCs: $\Gamma_{ET} = 1/\langle \tau_{hop} \rangle = \langle n_{hop} \rangle / \tau_{FL}^{fast} = 1/0.089 = 11.3\ ns^{-1}$.

The short-chain MPA linkers are well suited for applications requiring high photoconductivity of a NC solid. Alternatively, light-emitting properties of NCs are enhanced in solids with larger interparticle gaps.[13] In this work, we explore the exciton dynamics of weakly coupled films by cross-linking PbS NCs with long-chain MOA ligands. For these molecules, the edge-to-edge interparticle gap is 1.7 nm, corresponding to a l_{hop} value of 4.8 nm.[13] The greater interparticle separation for MOA-linked solids is expected to cause a slower diffusion of excitons throughout the film. Likewise, the dissociation rate of excitons in MOA-linked solids will be reduced compared to MPA-linked films due to an increased potential barrier between adjacent dots.[40,44] This trend is clearly seen in the FL intensity decay of MOA-linked PbS NC solids. According to Figure 6a, the fast component of the emission lifetime (τ_{fast} (MOA) = 15.1 ns) in PbS-only solids is substantially longer than that of MPA-linked films (τ_{fast}(MPA) = 1.1 ns), reflecting a slower rate of exciton dissociation. With the addition of Au NPs the fast component of the emission lifetime in MOA-linked films (R_{Au-Au} = 24.9 nm; $l_{free\ travel}$ = 8.8 nm) decreases from 15.1 to 6.7 ns due to quenching. By using the aforementioned strategy (Figure 6b), we estimate the single-hop dissociation probability for MOA-linked films using three concentrations of Au in PbS NC solids (see Supporting Information, Table ST2). The average dissociation probability was found to be p_{diss}(1 hop) $\approx$ 0.03, corresponding to an average number of interparticle hops, $\langle n_{hop} \rangle$, of 34 (see Table 1). The associated diffusion length was 11.4 nm.

The increased amount of interparticle hops in NC solids featuring weaker electrical coupling is consistent with the previously proposed charge-tunneling mechanism of the exciton dissociation.[44] Indeed, if the ionization of excitons is driven by trapping on nanoparticle surfaces, then $\langle n_{hop}$(MOA)$\rangle$ should be significantly smaller than $\langle n_{hop}$(MPA)$\rangle$ since the density of traps is roughly the same for both film types while diffusion in MOA-linked films is much slower. However, if the dissociation event occurs due to tunneling of one of the charges to a neighboring nanoparticle or a remote defect state, $\langle n_{hop}$(MOA)$\rangle$ could, in principle, be greater than $\langle n_{hop}$(MPA)$\rangle$. This scenario is possible when the rate of nonresonant charge tunneling to a different NC drops faster with an increasing interparticle gap than the rate of resonant energy transfer between neighboring dots. Consequently, the observed increase in the number of interparticle hops upon MPA → MOA ligand exchange provides additional evidence supporting the charge tunneling mechanism of exciton dissociation.

The PbS-to-PbS energy transfer rate for MOA-linked solids was found to be $1/0.44 = 2.3\ ns^{-1}$ (see Table 1), approximately an order of magnitude slower than in the case of short-chain MPA ligands. Notably, the 0.089 → 0.44 ns increase in the hopping time was caused by the 4.0 → 4.8 nm enhancement in the center-to-center interparticle distance. If we assume a power dependence of the ET rate on the donor−acceptor distance, $\sim(l_{hop})^{\alpha}$, then the best fit is obtained for $\alpha = 8.7$. Given a large uncertainty associated with only two data points (R_{MPA} and R_{MOA}), it is difficult to tell whether the observed scaling deviates from the $\alpha = 6$ Förster power dependence. However, it should be noted that a possibility of such non-Förster *R*-dependence of the

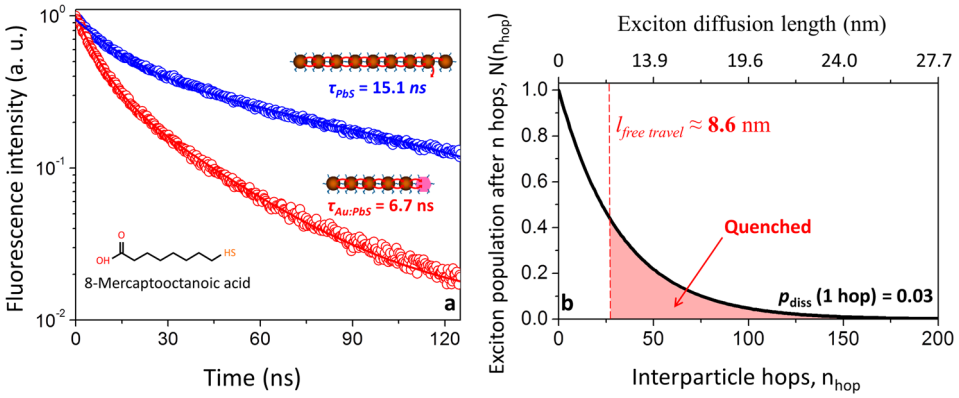

Figure 6. Experimental determination of the exciton diffusion length in MOA-linked PbS NC solids. (a) The FL intensity decay of PbS-only (blue) and doped (Au+PbS) NC solids (red). The reduction in the fast decay component due to Au doping (Au:PbS = 1:55 by count) by a factor of 6.7/15.1 is attributed to forced dissociation. (b) Modeling of the exciton population curve (N(p_{diss}(1)) corresponding to the experimentally observed reduction in the fast FL decay component. Here, p_{diss}(1 hop) = 0.03.

energy transfer in NC assemblies has been acknowledged in a number of recent reports.[36,60]

To further explore the nature of exciton dissociation processes the time-resolved data were complemented with the analysis of the steady-state emission in Au-doped films. Because of the diffusion of excitons toward the potential minima, the emission of solid-bound NCs is typically red-shifted relative to the corresponding maximum in solution.[61] By adding Au NPs to the solid, we can controllably lower the diffusion volume of excitons, which should cause the magnitude of the emission red-shift to diminish. This strategy can therefore be used to map the average distribution of excitonic traps—large-diameter PbS NCs that funnel the exciton energy. Notably, the comparison of the emission changes between PbS-only and Au-doped solids provides a more accurate description of energy funneling process than the one obtained through the comparison of emission maxima between nanoparticles in solution and solid forms, since the effect of solvent charging and wave function delocalization are excluded.

Figure 7 shows the steady-state emission of PbS-only (red) and two mixed (PbS, Au) films cross-linked with MPA ligands. The emission maxima of Au-doped solids are blue-shifted relative to the FL peak of PbS-only films, as expected due to the restricted volume of the exciton diffusion in the former case. The maximum magnitude of the spectral shift is obtained at high levels of Au doping (R_{Au-Au} = 14.6 nm; exciton mean free path, $l_{free\ \ travel}$ = 6.8 nm) and equals to $\Delta\lambda$ = 4 nm (5.5 meV). Considering that NCs are electrically coupled if the energy disorder in the film is lower than $\Delta E \ll 2(2\Delta kT)^{1/2} \approx 30$ meV, we conclude that the motion of excitons in the investigated PbS NC film is rather random at room temperature. Consequently, quantum funneling is not likely to be prevalent in MPA-linked PbS films featuring a small dispersion of nanoparticle diameters. The lack of a significant energy gradient in PbS NC solids is consistent with the proposed charge-tunneling mechanism of the exciton dissociation.

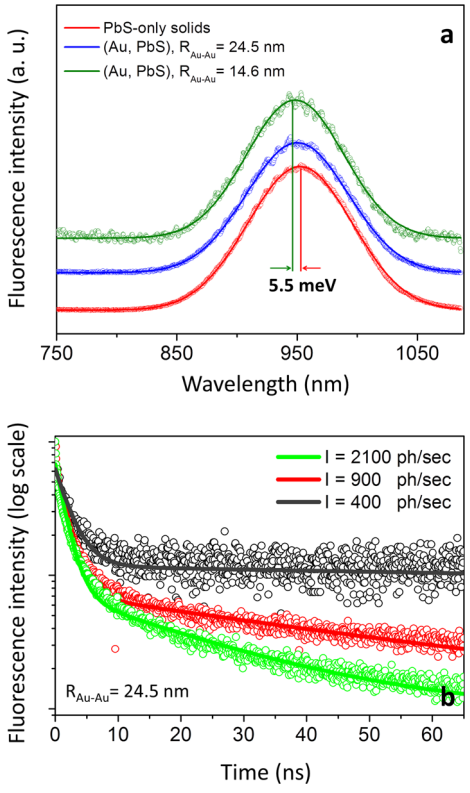

Figure 7. (a). The steady-state emission of PbS NC solids doped with Au nanoparticles. The blue shift of the emission is attributed to the forced dissociated in Au-doped films, which shortens the diffusion length whereby excitons are prevented from reaching the local potential minima in the film. (b). The excitation power dependence of the FL intensity decay in PbS-only NC solids. The slow decay component appears to be strongly affected by the excitation intensity, which is consistent with the proposed free-career origin of this decay channel.

This process is independent of the energy disorder and can lead to the dissociation of excitons even in a solid of identical NCs. Consequently, we can assume that the exciton dissociation probability is the probability of charge tunneling (ionization), as was suggested by the work of Guyot-Sionnest.[62] That is p_{diss}(MPA) = 0.09 is the

probability of electron tunneling per single interparticle hop.

While the fast component of the FL intensity decay reflects the rate of exciton dissociation processes, the slow exponent has been tentatively attributed to the recombination of free carriers in a NC solid.[44] If this assignment is correct, the slow decay component will be shortened as a result of Au doping since metal nanoparticles are likely to absorb the excited charges. From the broader prospective, we expect the decay of photoinduced carriers in Au-doped films to be determined by the two competing processes: radiative recombination, which depends on the concentration of free carriers in a solid, and trapping of charges, which is determined by Au-doping. The contribution of the former process is clearly seen in the comparison of the PbS-only and Au-doped films in Figure 6a. The slow component of the FL decay decreases from 150 to 32 ns upon the addition of Au NPs (R_{Au-Au} = 24.3 nm), which reflects an efficient consumption of free carriers by Au NPs. Using a previously developed model,[44] we estimate the average diffusion length of free carriers in terms of the slow and the fast components of the FL intensity decay: $l_{diff}^{free\ \ carrier} = l_{step} \times (\tau_{FL,slow}/6\tau_{FL,fast})^{1/2}$. In the case of MPA-linked PbS solids (Figure 7b, green curve), the value of $l_{diff}^{free\ \ carrier}$ is 5.3 nm. Notably, the average mean free path of free carriers in MPA-linked films estimated from the Au−Au interparticle distance, $l_{free\ \ travel}$, (which in the absence of the electric field will be the same as for neutral excitons) is ≈ 7 nm. This value is in a good agreement with the extracted $l_{diff}^{free\ \ carrier}$ of 5.3 nm, considering that the former figure is likely to be revised lower when the contribution of intrinsic (non-Au) traps is included. The observed reduction of the τ_{slow} lifetime in Au-doped solids provides additional evidence in support of the proposed free-carrier origin of the slow decay component in PbS NC solids. This assignment is further confirmed by the excitation power dependence of the $1/\tau_{slow}$ rate in undoped PbS NC solids. According to Figure 7b, the rise in the excitation power leads to the increase in the rate of the slow decay component while the fast component remains nearly the same. The dependence of τ_{slow} on the excitation intensity is consistent with the free-carrier mechanism of the FL decay since the recombination rate of free carriers is strongly dependent on their concentration in a solid.

CONCLUSIONS

We have demonstrated a spectroscopic approach for mapping the ultrafast dynamics of excitons in NC solids with a subdiffraction spatial resolution. By introducing Au nanoparticles into NC films the motion of excitons was restricted to a well-defined volume. The exciton diffusion beyond this volume resulted in quenching of the fluorescence and was detected as a change in the emission lifetime. Here, this strategy was employed for studying the exciton dynamics in two types of PbS NC solids featuring both strong (MPA-linked) and weak (MOA-linked) interparticle coupling. These measurements allowed a determination of a number of important transport characteristics including the exciton diffusion length, the rate of energy transfer between neighboring PbS dots, the number of interparticle hops performed by excitons prior to the dissociation, and the ensuing exciton diffusivity. In the case of MPA-linked solids excitons were found to diffuse to an average length of 5.7 nm in approximately 12 hops, which corresponded to the diffusivity of 0.012 $cm^2\ s^{-1}$. Meanwhile, MOA-linked solids gave rise to a longer diffusion length of 11.4 nm (34 hops) and a lower diffusivity of 0.003 $cm^2\ s^{-1}$. The observed difference in the dynamics of the two film types was consistent with the proposed charge-tunneling mechanism of the exciton dissociation. The developed experimental strategy was also extended for imaging the diffusion of free carriers that emerge as a result of exciton diffusion. We expect that the demonstrated imaging strategy will avail the rational design of NC devices, where interface-limited diffusion of excitons is critical to the performance. These include NC solar cells, light-emitting diodes, and photodetectors.

METHODS

Materials. Lead(II) oxide powder (PbO, 99.999% Aldrich), 1-octadecene (ODE, 90% Aldrich), oleic acid (OA, 90% Aldrich), bis-(trimethylsilyl) sulfide ($(TMS)_2S$, Aldrich, synthetic grade), acetone (anhydrous Amresco, ACS grade), hexane (anhydrous, 95% Aldrich), ethanol (anhydrous, 95% Aldrich), methanol (anhydrous, 99.8% Aldrich), isopropyl alcohol (anhydrous, 99.8% Acros), toluene (anhydrous, 99.8% Aldrich), 3-mercaptopropionic acid (MPA, 99%, Alfa Aesar), 8-mercaptooctanoic acid (MOA, 95%, Aldrich), gold(III) chloride ($AuCl_3$ 99%, Acros Organics) were used as received without any further purification. Oleylamine (tech., 70%, Aldrich) was pumped for 1 h at 120 °C and then stored under argon atmosphere prior to use. Fluorine-doped tin oxide (FTO, SnO_2/F) glass (TEC 15, 12−14 Ohm/sq) was obtained from Pilkington Glass. All reactions were performed under argon atmosphere using the standard Schlenk technique. The centrifuge used for precipitation operated at 7200 rpm.

Synthesis of PbS NCs. PbS NCs were fabricated according to a procedure adapted from Hines *et al.*[63] In a typical synthesis, a mixture of 0.49 g (2 mmol) of PbO in 18 mL of ODE and 1−16 mL of OA (increasing the amount of OA results in a larger NC diameter) was degassed in a three-neck flask at 120 °C for 2 h, switched to argon, and heated to 135 °C. Meanwhile, 10 mL of ODE was degassed for 2 h at 120 °C and allowed to cool down to room temperature. Then, 0.21 mL of $(TMS)_2S$ was added carefully into the flask, and the resulting $(TMS)_2S$/ODE mixture was injected into the Pb precursor solution at 135 °C, while stirring. The reaction was stopped after 0−5 min (longer reaction time leads to larger NCs) by removing the flask from the heating mantle and placing it into an ice water bath. Nanocrystals were isolated from the mixture by precipitating with acetone,

centrifuging, and redispersing in toluene. The cleaning procedure was repeated 2−3 times, upon which NCs were redispersed in a minimal amount of hexane (4−5 mL).

For example, to fabricate PbS NCs with an exciton absorption feature centered at 930 nm (d_{PbS} = 3.0 nm), 1.5 mL of OA was used with the reaction time of 1 min. For NCs with a 1s peak at 1050 nm (d_{PbS} = 3.5 nm), 2 mL of OA was used, and the growth time was limited to 1 min. For NCs with a 1s peak at 1300 nm (d_{PbS} = 4.6 nm), 14 mL of OA was used with the growth time of 4 min.

Synthesis of Oleylamine-Capped Au NCs. Au NCs were synthesized according to a previously reported methodology.[64] In a typical synthesis, 0.011 g of $AuCl_3$ and 5 mL of oleylamine were loaded in a one-neck flask and allowed to react at 100 °C for 30 min under argon atmosphere. During this time, the reaction mixture's color changed from transparent yellow to orange (indicating the formation of Au-oleate complexes), and then finally to purple (indicating the formation of oleylamine-capped Au NPs). The reaction was stopped by removing the flask from the heating mantle and allowing it to cool to room temperature. Then, the solution was transferred from the flask into centrifuge tubes and precipitated with ethanol. After the centrifugation, the supernatant was discarded and the pellet was dissolved in chloroform. The cleaning cycle was repeated one more time and the final product was redispersed and stored in 5 mL of chloroform. The final product contained Au NPs with an average diameter of 5 nm and a surface plasmon resonance (LSPR) peak at $\lambda \approx 525$ nm.

Preparation of the NC Film. MPA-linked PbS NC films were deposited using a layer-by-layer spin-coating process under an argon atmosphere. For each layer, the solution of PbS NCs in hexane (concentration 20 mg/mL) or a mixture of PbS and Au NCs was deposited on the glass substrate and spun at 3000 rpm for 10 s. Subsequently, 7−10 drops of MPA/methanol solution (ratio = 1:4) were deposited on the center of the glass slide, soaked for 10 s and spun at 3000 rpm for 10 s. Finally, the film was rinsed with methanol and hexane solutions. The total amount of layers varied from 3 to 4. Ratios of PbS to Au were calculated using a volume fraction of each material in the mixture (see the Supporting Information).

MOA-linked NC solids were fabricated using a layer-by-layer spin-coating process under an argon atmosphere. After the deposition of 5−7 drops of PbS NCs, or a mixture of PbS and Au NCs, onto a FTO/glass substrate followed by spinning at 3000 rpm for 15 s, the film was immersed into 0.7 M MOA solution in acetonitrile for 1 min and washed with 10 drops of acetonitrile. Overall, 3−4 cycles were required to completely perform the deposition of PbS or PbS/Au NCs. Ratios of PbS with Au for the mixed films were calculated the same way as in the case of MPA-linked films.

Characterization. Absorbance spectra were recorded using CARY 50 scan and Simadzu UV-3600 UV−vis−NIR spectrophotometers. Photoluminescence spectra were recorded using a Jobin Yvon Fluorolog FL3-11 fluorescence spectrophotometer. High-resolution transmission electron microscopy (HR-TEM) measurements were carried out using JEOL 3011UHR and 2010 transmission electron microscopes, operated at 300 and 200 kV, respectively. To prepare a TEM sample, a small amount of NC film was scraped, dispersed in toluene by sonication, dropped onto a carbon-coated copper grid, and allowed to dry in air. X-ray powder diffraction (XRD) measurements were carried out on a Scintag XDS-2000 X-ray powder diffractometer. FL lifetime measurements were performed using a time-correlated single photon counting setup utilizing SPC-630 single-photon counting PCI card (Becker & Hickle GmbH), picosecond diode laser operating at 400 nm, as an excitation source (Picoquant), an id50 avalanche photodiode (Quantique), and long pass filters on 400 nm and 532 nm.

Conflict of Interest: The authors declare no competing financial interest.

Acknowledgment. We gratefully acknowledge OBOR "Material Networks" program and NSF Awards CHE-1112227 and CBET-1236355 for financial support. P.M. was supported by a McMaster Fellowship. J.B. and M.S. were funded by the Welch foundation Grant No. U-0047.

Supporting Information Available: Experimental details, additional TEM images. This material is available free of charge *via* the Internet at http://pubs.acs.org.

REFERENCES AND NOTES

1. Baumgardner, W. J.; Whitham, K.; Hanrath, T. Confined-but-Connected Quantum Solids *via* Controlled Ligand Displacement. *Nano Lett.* **2013**, *13*, 3225–3231.
2. Nag, A.; Kovalenko, M. V.; Lee, J.-S.; Liu, W.; Spokoyny, B.; Talapin, D. V. Metal-Free Inorganic Ligands for Colloidal Nanocrystals: S^{2-}, HS^-, Se^{2-}, HSe^-, Te^{2-}, HTe^-, TeS_3^{2-}, OH^- and NH_2^- as Surface Ligands. *J. Am. Chem. Soc.* **2011**, *133*, 10612–10620.
3. Norman, Z. M.; Anderson, N. C.; Owen, J. S. Electrical Transport and Grain Growth in Solution-Cast, Chloride-Terminated Cadmium Selenide Nanocrystal Thin Films. *ACS Nano* **2014**, *8*, 7513–7521.
4. Lee, J. S.; Kovalenko, M. V.; Huang, J.; Chung, D. S.; Talapin, D. V. Band-like Transport, High Electron Mobility and High Photoconductivity in All-Inorganic Nanocrystal Arrays. *Nat. Nanotechnol.* **2011**, *6*, 348–352.
5. Dong, A.; Jiao, Y.; Milliron, D. J. Electronically Coupled Nanocrystal Superlattice Films by *in Situ* Ligand Exchange at the Liquid−Air Interface. *ACS Nano* **2013**, *7*, 10978–10984.
6. Webber, D. H.; Brutchey, R. L. Ligand Exchange on Colloidal CdSe Nanocrystals Using Thermally Labile *tert*-Butylthiol for Improved Photocurrent in Nanocrystal Films. *J. Am. Chem. Soc.* **2012**, *134*, 1085–1092.
7. Kinder, E.; Moroz, P.; Diederich, G.; Johnson, A.; Kirsanova, M.; Nemchinov, A.; O'Connor, T.; Roth, D.; Zamkov, M. Fabrication of All-Inorganic Nanocrystal Solids through Matrix Encapsulation of Nanocrystal Arrays. *J. Am. Chem. Soc.* **2011**, *133*, 20488–20499.
8. Khon, E.; Lambright, S.; Khon, D.; Smith, B.; O'Connor, T.; Moroz, P.; Imboden, M.; Diederich, G.; Perez-Bolivar, D.; Anzenbacher, P.; *et al.* Inorganic Solids of CdSe Nanocrystals Exhibiting High Emission Quantum Yield. *Adv. Funct. Mater.* **2012**, *22*, 3714–3722.
9. Liu, Y.; Tolentino, J.; Gibbs, M.; Ihly, R.; Perkins, C. L.; Liu, Y.; Crawford, N. R. M.; Hemminger, J. C.; Law, M. PbSe Quantum Dot Field-Effect Transistors with Air-Stable Electron Mobilities above 7 $cm^2 V^{-1} s^{-1}$. *Nano Lett.* **2013**, *13*, 1578–1587.
10. Ihly, R.; Tolentino, J.; Liu, Y.; Gibbs, M.; Law, M. The Photothermal Stability of PbS Quantum Dot Solids. *ACS Nano* **2011**, *5*, 8175–8186.
11. Colvin, V. L.; Schlamp, M. C.; Alivisatos, A. P. Light-Emitting Diodes Made from Cadmium Selenide Nanocrystals and a Semiconducting Polymer. *Nature* **1994**, *370*, 354–357.
12. Coe, S.; Woo, W. K.; Bawendi, M.; Bulovic, V. Electroluminescence from Single Monolayers of Nanocrystals in Molecular Organic Devices. *Nature* **2002**, *420*, 800–803.
13. Sun, L.; Choi, J. J.; Stachnik, D.; Bartnik, A. C.; Hyun, B.-R.; Malliaras, G. G.; Hanrath, T.; Wise, F. W. Bright Infrared Quantum-Dot Light-Emitting Diodes through Inter-dot Spacing Control. *Nat. Nanotechnol.* **2012**, *7*, 369–373.
14. Shirasaki, Y.; Supran, G. J.; Bawendi, M. G.; Bulovic, V. Emergence of Colloidal Quantum-Dot Light-Emitting Technologies. *Nat. Photonics* **2013**, *7*, 13–23.
15. Talapin, D. V.; Lee, J. S.; Kovalenko, M. V.; Shevchenko, E. V. Prospects of Colloidal Nanocrystals for Electronic and Optoelectronic Applications. *Chem. Rev.* **2010**, *110*, 389–458.
16. Son, D. I.; Kwon, B. W.; Park, D. H.; Seo, W. S.; Yi, Y.; Angadi, B.; Lee, C. L.; Choi, W. K. Emissive ZnO-Graphene Quantum Dots for White-Light-Emitting Diodes. *Nat. Nanotechnol.* **2012**, *7*, 465–471.
17. Chen, O.; Wei, H.; Maurice, A.; Bawendi, M. G.; Reiss, P. Pure Colors from Core−Shell Quantum Dots. *MRS Bull.* **2013**, *38*, 696–702.

18. Supran, G. J.; Shirasaki, K. W.; Song, K. W.; Caruge, J.-M.; Kazlas, P. T.; Coe-Sullivan, S.; Andrew, T. L.; Bawendi, M. G.; Bulovic, V. QLEDs for Displays and Solid-State Lighting. *MRS Bull.* **2013**, *38*, 703–711.
19. Tang, J.; Kemp, K. W.; Hoogland, S.; Jeong, K. S.; Liu, H.; Levina, L.; Furukawa, M.; Wang, X.; Debnath, R.; Cha, D.; *et al*. Colloidal-Quantum-Dot Photovoltaics Using Atomic-Ligand Passivation. *Nat. Mater.* **2011**, *10*, 765–771.
20. Huynh, W. U.; Dittmer, J. J.; Alivisatos, A. P. Hybrid Nanorod-Polymer Solar Cells. *Science* **2002**, *295*, 2425–2427.
21. Gur, I.; Fromer, N. A.; Geier, M. L.; Alivisatos, A. P. Air-Stable All-Inorganic Nanocrystal Solar Cells Processed from Solution. *Science* **2005**, *310*, 462–465.
22. Erickson, C. S.; Bradshaw, L. R.; McDowall, S.; Gilbertson, J. D.; Gamelin, D. R.; Patrick, D. L. Zero-Reabsorbtion Doped-Nanocrystal Luminescent Solar Concentrators. *ACS Nano* **2014**, *8*, 3461–3467.
23. Semonin, O. E.; Luther, J. M.; Choi, S.; Chen, H.-Y.; Gao, J.; Nozik, A. J.; Beard, M. C. Peak External Photocurrent Quantum Efficiency Exceeding 100% *via* MEG in a Quantum Dot Solar Cell. *Science* **2011**, *334*, 1530–1533.
24. Ip, A. H.; Thon, S. M.; Hoogland, S.; Voznyy, O.; Zhitomirsky, D.; Debnath, R.; Levina, L.; Rollny, L. R.; Carey, G. H.; Fischer, A.; *et al*. Hybrid Passivated Colloidal Quantum Dot Solids. *Nat. Nanotechnol.* **2012**, *7*, 577–582.
25. Kramer, I. J.; Sargent, E. H. Colloidal Quantum Dot Photovoltaics: A Path Forward. *ACS Nano* **2011**, *5*, 8506–8514.
26. Sargent, E. H. Colloidal Quantum Dot Solar Cells. *Nat. Photonics* **2012**, *6*, 133–135.
27. Kramer, I. J.; Levina, L.; Debnath, R.; Zhitomirsky, D.; Sargent, E. H. Solar Cells Using Quantum Funnels. *Nano Lett.* **2011**, *11*, 3701–3706.
28. Tang, J.; Liu, H.; Zhitomirsky, D.; Hoogland, S.; Wang, X.; Furukawa, M.; Levina, L.; Sargent, E. H. Quantum Junction Solar Cells. *Nano Lett.* **2012**, *12*, 4889–4894.
29. Kamat, P. V. Quantum Dot Solar Cells. Semiconductor Nanocrystals as Light Harvesters. *J. Phys. Chem.C* **2008**, *112*, 18737–18753.
30. Pattantyus-Abraham, A. G.; Kramer, I. J.; Barkhouse, A. R.; Wang, X.; Konstantatos, G.; Debnath, R.; Levina, L.; Raabe, I.; Nazeeruddin, M. K.; Grätzel, M.; *et al*. Depleted- Heterojunction Colloidal Quantum Dot Solar Cells. *ACS Nano* **2010**, *4*, 3374–3380.
31. Keuleyan, S.; Lhuillier, E.; Brajuskovic, V.; Guyot-Sionnest, P. Mid-infrared HgTe Colloidal Quantum Dot Photodetectors. *Nat. Photonics* **2011**, *5*, 489–493.
32. Konstantatos, G.; Badioli, M.; Gaudreau, L.; Osmond, J.; Bernechea, M.; de Arquer, F. P. G.; Gatti, F.; Koppens, F. H. L. Hybrid Graphene-Quantum Dot Phototransistors with Ultrahigh Gain. *Nat. Nanotechnol.* **2012**, *7*, 363–368.
33. Konstantatos, G.; Howard, I.; Fischer, A.; Hoogland, S.; Clifford, J.; Klem, E.; Levina, L.; Sargent, E. H. Ultrasensitive Solution-Cast Quantum Dot Photodetectors. *Nature* **2006**, *442*, 180–183.
34. Chuang, C. H. M.; Brown, P. R.; Bulovic, V.; Bawendi, M. G. Improved Performance and Stability in Quantum Dot Solar Cells through Band Alignment Engineering. *Nat. Mater.* **2014**, *13*, 796–801.
35. Akselrod, G. M.; Prins, F.; Poulikakos, L. V.; Lee, E. M.; Weidman, M. C.; Mork, A. J.; Willard, A. P.; Bulović, V.; Tisdale, W. A. Subdiffusive Exciton Transport in Quantum Dot Solids. *Nano Lett.* **2014**, *14*, 3556–3562.
36. Mork, A. J.; Weidman, M. C.; Prins, F.; Tisdale, W. A. Magnitude of the Förster Radius in Colloidal Quantum Dot Solids. *J. Phys. Chem. C* **2014**, *118*, 13920–13928.
37. Graetzel, M.; Janssen, R. A. J.; Mitzi, D. B.; Sargent, E. H. Materials Interface Engineering for Solution-Processed Photovoltaics. *Nature* **2012**, *488*, 304–312.
38. Thompson, N. J.; Wilson, M. W. B.; Congreve, D. N.; Brown, P. R.; Scherer, J. M.; Bischof, T. S.; Wu, M.; Geva, N.; Welborn, M.; Voorhis, T. V.; *et al*. Energy Harvesting of Non-emissive Triplet Excitons in Tetracene by Emissive PbS Nanocrystals. *Nat. Mater.* **2014**, *13*, 1039–1043.
39. Mashford, B.; Stevenson, M.; Popovic, Z.; Hamilton, C.; Zhou, Z.; Breen, C.; Steckel, J.; Bulović, V.; Bawendi, M. G.; Coe-Sullivan, S.; *et al*. High-Efficiency Quantum-Dot Light-Emitting Devices with Enhanced Charge Injection. *Nat. Photonics* **2013**, *7*, 407–412.
40. Choi, J. J.; Luria, J.; Hyun, B.-R.; Bartnik, A. C.; Sun, L.; Lim, Y.- F.; Marohn, J. A.; Wise, F. W.; Hanrath, T. Photogenerated Exciton Dissociation in Highly Coupled Lead Salt Nanocrystal Assemblies. *Nano Lett.* **2010**, *10*, 1805–1811.
41. Liu, Y.; Gibbs, M.; Puthussery, J.; Gaik, S.; Ihly, R.; Hillhouse, H. W.; Law, M. Dependence of Carrier Mobility on Nanocrystal Size and Ligand Length in PbSe Nanocrystal Solids. *Nano Lett.* **2010**, *10*, 1960–1969.
42. Kovalenko, M. V.; Scheele, M.; Talapin, D. V. Colloidal Nanocrystals with Molecular Metal Chalcogenide Surface Ligands. *Science* **2009**, *324*, 1417–1420.
43. Talgorn, E.; Gao, Y.; Aerts, M.; Kunneman, L. T.; Schins, J. M.; Savenije, T. J.; van Huis, M. A.; van der Zant, H. S. J.; Houtepen, A. J.; Siebbeles, L. D. A. Unity Quantum Yield of Photogenerated Charges and Bandlike Transport in Quantum-Dot Solids. *Nat. Nanotechnol.* **2011**, *6*, 733–739.
44. Moroz, P.; Kholmicheva, N.; Mellott, B.; Liyanage, G.; Rijal, U.; Bastola, E.; Huband, K.; Khon, E.; McBride, K.; Zamkov, M. Suppressed Carrier Scattering in CdS-Encapsulated PbS Nanocrystal Films. *ACS Nano* **2013**, *7*, 6964–6977.
45. Fafarman, A. T.; Koh, W. K.; Diroll, B. T.; Kim, D. K.; Ko, D. K.; Oh, S. J.; Ye, X. C.; Doan-Nguyen, V.; Crump, M. R.; Reifsnyder, D. C.; *et al*. Thiocyanate-Capped Nanocrystal Colloids: Vibrational Reporter of Surface Chemistry and Solution-Based Route to Enhanced Coupling in Nanocrystal Solids. *J. Am. Chem. Soc.* **2011**, *133*, 15753–15761.
46. Zhitomirsky, D.; Voznyy, O.; Levina, L.; Hoogland, S.; Kemp, K. W.; Ip, A. H.; Thon, S. M.; Sargent, E. H. Engineering Colloidal Quantum Dot Solids within and beyond the Mobility-Invariant Regime. *Nat. Commun.* **2014**, *5*, 3803.
47. Kagan, C.; Murray, C.; Bawendi, M. G. Long-Range Resonance Transfer of Electronic Excitations in Close-Packed CdSe Quantum-Dot Solids. *Phys. Rev.* **1996**, *54*, 8633–8643.
48. Crooker, S.; Hollingsworth, J.; Tretiak, S.; Klimov, V. Spectrally Resolved Dynamics of Energy Transfer in Quantum-Dot Assemblies: Towards Engineered Energy Flows in Artificial Materials. *Phys. Rev. Lett.* **2002**, *89*, 186802.
49. Zhitomirsky, D.; Voznyy, O.; Hoogland, S.; Sargent, E. H. Measuring Charge Carrier Diffusion in Coupled Colloidal Quantum Dot Solids. *ACS Nano* **2013**, *7*, 5282–5290.
50. Gao, Y.; Sandeep, C. S. S.; Schins, J. M.; Houtepen, A. J.; Siebbeles, L. D. A. Disorder Strongly Enhances Auger Recombination in Conductive Quantum-Qot Solids. *Nat. Commun.* **2013**, *4*, 2329.
51. Gao, Y.; Talgorn, E.; Aerts, M.; Trinh, M. T.; Schins, J. M.; Houtepen, A. J.; Siebbeles, L. D. A. Enhanced Hot-Carrier Cooling and Ultrafast Spectral Diffusion in Strongly Coupled PbSe Quantum-Dot Solids. *Nano Lett.* **2011**, *11*, 5471–5476.
52. Crisp, R. W.; Schrauben, J. N.; Beard, M. C.; Luther, J. M.; Johnson, J. C. Coherent Exciton Delocalization in Strongly Coupled Quantum Dot Arrays. *Nano Lett.* **2013**, *13*, 4862–4869.
53. Jennings, T. L.; Singh, M. P.; Strouse, G. F. Fluorescent Lifetime Quenching Near $d = 1.5$ nm Gold Nanoparticles: Probing NSET Validity. *J. Am. Chem. Soc.* **2006**, *128*, 5462–5467.
54. Breshike, C. J.; Riskowski, R. A.; Strouse, G. F. Leaving Foerster Resonance Energy Transfer Behind: Nanometal Surface Energy Transfer Predicts Size-Enhanced Energy Coupling between Metal Nanoparticle and Emitting Dipole. *J. Phys. Chem. C* **2013**, *117*, 23942–23949.
55. Curutchet, C.; Franceschetti, A.; Zunger, A.; Scholes, G. D. Examining Förster Energy Transfer for Semiconductor Nanocrystalline Quantum Dot Donors and Acceptors. *J. Phys. Chem. C* **2008**, *112*, 13336–13341.
56. Xu, F.; Ma, X.; Haughn, C. R.; Benavides, J.; Doty, M. F.; Cloutier, S. G. Efficient Exciton Funneling in Cascaded PbS Quantum Dot Superstructures. *ACS Nano* **2011**, *5*, 9950–9957.
57. Moroz, P.; Liyanage, G.; Kholmicheva, N.; Yakunin, S.; Uprety, P.; Bastola, E.; Rijal, U.; Mellott, B.; Subedi, K.;

Sun, L.; *et al*. Infrared Emitting PbS Nanocrystal Solids through Matrix Encapsulation. *Chem. Mater.* **2014**, *26*, 4256–4264.
58. Powell, R. C.; Soos, Z. G. Singlet exciton energy transfer in organic solids. *J. Lumin.* **1975**, *11*, 1–45.
59. Gao, J.; Zhang, J.; van de, Lagemaat.; Johnson, J. C.; Beard, M. C. Charge Generation in PbS Quantum Dot Solar Cells Characterized by Temperature-Dependent Steady-State Photoluminescence. *ACS Nano* **2014**, *8*, 12814–12825.
60. Curutchet, C.; Franceschetti, A.; Zunger, A.; Scholes, G. D. Examining Förster Energy Transfer for Semiconductor Nanocrystalline Quantum Dot Donors and Acceptors. *J. Phys. Chem. C* **2008**, *112*, 13336–13341.
61. Luther, J. M.; Law, M.; Song, Q.; Perkins, C. L.; Beard, M. C.; Nozik, A. J. Structural, Optical, and Electrical Properties of Self-Assembled Films of PbSe Nanocrystals Treated with 1,2-Ethanedithiol. *ACS Nano* **2008**, *2*, 271–280.
62. Guyot-Sionnest, P. Electrical Transport in Colloidal Quantum Dot Films. *J. Phys. Chem. Lett.* **2012**, *3*, 1169–1175.
63. Hines, M. A.; Scholes, G. D. Colloidal PbS Nanocrystals with Size-Tunable Near-Infrared Emission: Observation of Post-Synthesis Self-Narrowing of the Particle Size Distribution. *Adv. Mater.* **2003**, *15*, 1844–1849.
64. Khon, E.; Hewa-Kasakarage, N. N.; Nemitz, I.; Acharya, K. P.; Zamkov, M. Tuning the Morphology of Au/CdS Nanocomposites through Temperature-Controlled Reduction of Gold-Oleate Complexes. *Chem. Mater.* **2010**, *22*, 5929–5936.